2
Theory and Literature Review

2.1 Photovoltaic Effect

Solar panels, also known as photovoltaic devices, are used to convert sunlight into electricity. Edmond Becquerel is credited with discovering that when two metal electrodes were placed in a conducting medium, light might boost electricity generation. This innovation, known as the photovoltaic effect, is being advanced with selenium-based solar wafers. Bell Laboratory introduced silicon-based photovoltaic cells in 1954 (Chapin et al., 1954), resulting in a new revolution in the PV sector. When light irradiates, photons may get absorbed or pass through the absorber based on the absorber's bandgap and the photon energy. A solar cell is a p-n junction diode where no voltage is directly put across the junction. Figure 2.1 depicts the schematic of a p-n junction; even without bias, an electric field develops in the space charge area, referred to as the Built-in field. As photons illuminate the cell's surface, electron-hole pairs are generated in the space charge region and are swept out, resulting in reverse-biased photocurrent.

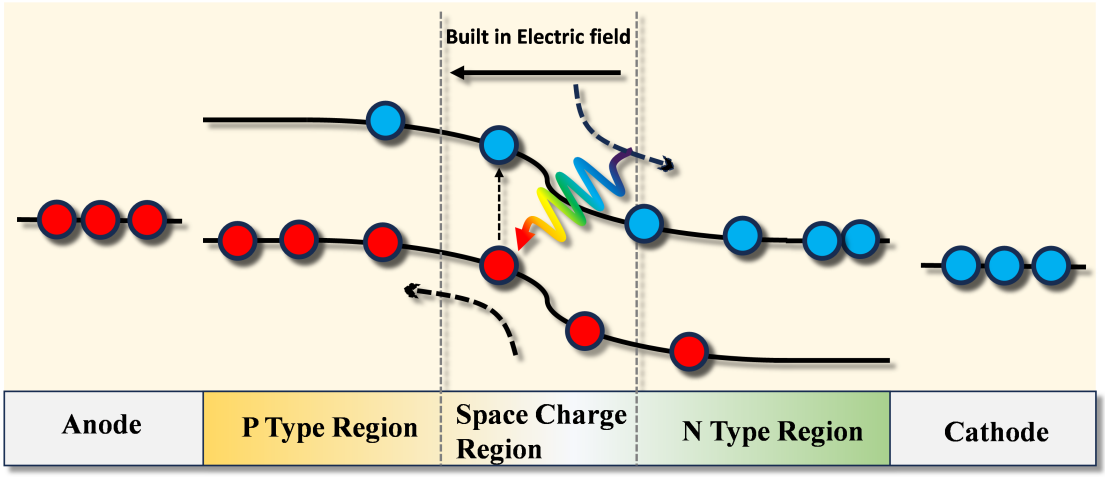


Figure 2.1 Schematic of a p-n junction. As photons illuminate the cell's surface, electron-hole pairs form and move in opposite direction due to built-in field present in the depletion region and get collected from the terminal.

2.2 Current transport in p-n junction diode

2.2.1 Under dark

In dark condition the value of current density in the semiconductor is given as

$$J = J_s\left[exp\left(\frac{eV}{nkT} - 1\right)\right] \tag{2.1}$$

$$with \;\; J_0 = en_i^2\left(\frac{D_n}{N_a L_n} + \frac{D_p}{N_d L_p}\right) \tag{2.2}$$

where L_n , L_p , D_n and D_p are diffusion length and diffusion constant of electrons and holes, respectively. The diode ideality factor "n" is 1 for an ideal p-n junction. Derivation of this equation requires the following assumptions: absence of generation or recombination currents inside the depletion layer, low injection conditions, Boltzmann approximation for charge carrier densities, and abrupt depletion layers. This diode equation is called the ideal diode equation or the Shockley equation.

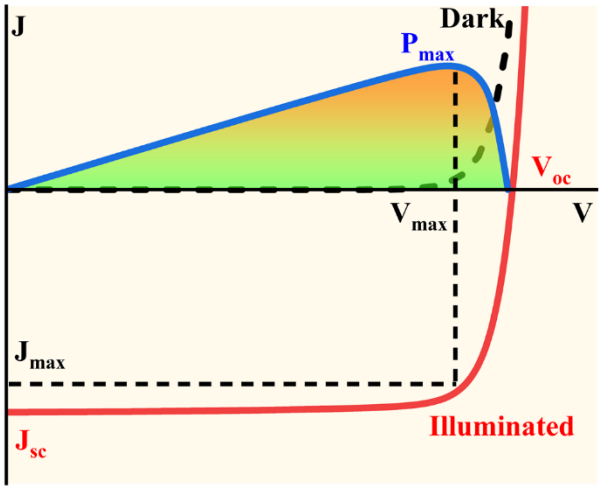


Figure 1.2 J-V characteristics of the dark and illuminated p-n junction.

2.2.2 Under illumination

When a p-n junction is exposed to light, additional electron-hole pairs are created in the semiconductor, resulting in a non-equilibrium condition due to unique quasi-fermi levels for both carriers. Next, minority carriers cross the depletion region and enter the quasi-neutral regions due to the substantial increase in their concentration on both the p and n regions, giving rise to a current known as photogenerated current density (J_{ph}). Furthermore, due to the separation of photogenerated carriers, a voltage difference is generated across the terminal, causing the junction to be self-forward biased. As a result, the net current density on the lighted pn-junction can be expressed as (Dieter K. Schroder, 2006);

$$J = J_F - J_{ph} = J_S \left[\exp\left(\frac{eV}{nkT}\right) - 1\right] - J_{ph} \tag{2.3}$$

As illustrated in Figure 2.2, the J-V characteristic of the p-n junction under light is the same as the dark J-V characteristic, but it is moved down by the photogenerated current J_{ph}. Further, the electric field amplitude in the space charge region drops when the diode becomes forward-biased, but it does not reach zero or change direction. For solar cell the photocurrent and the net current through the device remain reverse-biased. The short-circuit condition occurs when two terminals of solar cells are linked without external load resistance, R = 0, resulting in V = 0, and the current is known as the short-circuit current.; it is the maximum current produced by the cell in the absence of an external voltage and is stated as;

$$J = J_{sc} = -J_{ph} \tag{2.4}$$

The second limiting case is open-circuit condition and occurs when $R \rightarrow \infty$. The net current is zero, and the maximum voltage that can be produced is called the open-circuit voltage. Thus,

$$J = 0 = J_S \left[exp\left(\frac{eV_{oc}}{nkT}\right) - 1\right] - J_{ph} \tag{2.5}$$

The open circuit voltage V_{oc} is written as;

$$V_{oc} = \frac{kT}{e} \ln\left(1 + \frac{J_{ph}}{J_S}\right) \tag{2.6}$$

2.2.3 Conversion efficiency

If the load is connected to the terminal of the solar cell, then the power delivered to the load is;

$$P = J \,.V = J_S \left[\exp\left(\frac{eV}{nkT}\right) - 1\right].V - J_{ph}.V \tag{2.7}$$

The maximum power delivered to the load (P_{max}) occurs when the product J.V becomes maximum. By setting the derivative equal to zero, dP/dV = 0, and calling this voltage and current *Vm* and *Jm* values, we can see that the maximum delivered power is illustrated by the shaded region.

The conversion efficiency of a solar cell is defined as the ratio of output electrical power to incident optical power.

$$\eta = \frac{P_m}{P_{in}} \times 100\% = \frac{J_m V_m}{P_{in}} \times 100\ \% \quad = \frac{FF}{P_{in}} \times V_{oc}\, J_{sc} \times 100\ \% \tag{2.8}$$

where $\frac{J_m\, V_m}{J_{sc}\, V_{oc}} = FF$, is called the fill factor and is a figure of merit for solar cell design.

2.3 Shockley Queisser Limit

William Shockley and Hans-Joachim Queisser suggested a theoretical maximum solar cell efficiency for a single p-n junction in 1961 (W. H. Q. Shockley, 2011). The quantity of electrical energy extracted per incident photon is predicted to be 33.7 %, assuming a single p-n junction with a bandgap of 1.4 eV using AM 1.5 solar spectrum. This is referred to as the Shockley-Queisser limit or detailed balance limit. In general, device efficiency stays lower than this limit, such as 26% for crystalline silicon solar cells, 24% for CdTe-based cells, ~13% for CZTS-based solar cells, and so on. Nonideal effects, such as series resistance and reflection from the semiconductor surface, often reduce the photo conversion efficiency to 10 to 15%.

2.4 Solar Spectrum

The sun emits electromagnetic radiation with a wide range of wavelengths, from radio waves to infrared, visible, and ultraviolet to X-rays and gamma rays. Its distribution across the energy spectrum is similar to the black body radiation emitted at 6000 K. Depending on location and hours, it varies throughout the day. The tropics, for example, receive greater irradiance on average than the equator because clouds are less common, reflecting most of the incoming solar energy. Thus, even if the time of day and year were kept constant, comparing the performance of different solar cell technologies recorded in different locations would be extremely challenging due to variations in sun irradiation. Given this, a globally accepted reference for evaluating and comparing photovoltaic devices is chosen as the standard spectrum. In this series, air mass (AM) index is defined to measure the distance of light travelling through the atmosphere. The air mass and solar zenith angle are related through: $AM = \frac{1}{cos\theta_s}$

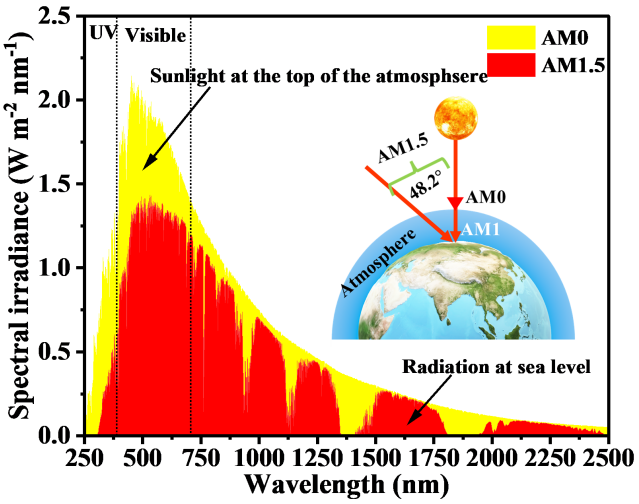


Figure 2.3 Spectral irradiance vs Wavelength AM 1.5 curve.

AM0 is a specific instance indicating that the light has not gone through any atmosphere and hence corresponds to light at the top of the atmosphere. This spectrum is used to evaluate solar cells intended for use in space, such as on satellites. AM 1.5 is used as the benchmark for terrestrial solar cell testing at 1000 W m^{-2} due to its fidelity to the annual mean irradiance in temperature latitudes, which are characterized by substantial population concentrations.

2.5 Charges in equilibrium and under illumination

The occupation of energy levels in a semiconductor is determined by the density of states and a distribution function. A current in a semiconductor can be contributed by two types of charge carriers: electrons and holes. Because the number of electrons in the conduction band and the number of holes in the valence band govern the current, the density of these charge carriers is very important. If n_0 and p_0 are the total concentrations of electrons and holes at thermal equilibrium, then(Neeman, 2012)

$$n_0 = \int_{E_c}^{\infty} g_c(E)\, f_F(E) dE \tag{2.9}$$

Where $f_F(E)$ is the Fermi-Dirac probability function, and $g_c(E)$ is the density of quantum states in the conduction band. The Fermi energy is assumed to be within the forbidden energy bandgap, therefore, for electrons in the conduction band, we have $E > E_c$. If $(E_c - E_F) >> kT$, then $(E - E_F) >> kT$, so that the Fermi probability function reduces to the Boltzmann approximation, which is

$$f_F(E) = \frac{1}{1 + \exp\dfrac{(E - E_F)}{kT}} \approx \exp\left[-\frac{(E - E_F)}{kT}\right] \tag{2.10}$$

Applying the Boltzmann approximation to equation 2.9, the thermal equilibrium density of electrons in the conduction band is found from

$$n_0 = \int_{E_c}^{\infty} \frac{4\pi(2m_n^*)^{\frac{3}{2}}}{h^3} \sqrt{E - E_c} \exp\left[-\frac{(E - E_F)}{kT}\right] dE \tag{2.11}$$

$$n_0 = N_c \exp\left[-\frac{(E - E_F)}{kT}\right] \tag{2.12}$$

Where, parameter N_c is called the effective density of states function in conduction band. If we assume m_n^* = m_0 then the the effective density of states function at T = 300 K is Nc = 2.5 ×10^{19} cm^{-3}, which is the order of magnitude of N_c for majority of the semiconductors. Similarly, the hole concentration in the valence band can be expressed as:

$$p_0 = N_v \exp\left[-\frac{(E_F - E_v)}{kT}\right] \tag{2.13}$$

Where N_v is called the effective density of states function in the valence band.
In an intrinsic semiconductor, the valence band hole concentration is equal to the conduction band electron concentration. $n_i = p_i$. Here the n_i and p_i are the electron and hole concentrations, respectively, in the intrinsic semiconductor. For intrinsic semiconductors we may write;

$$n_i^2 = N_c N_v \exp\left[-\frac{E_g}{kT}\right] \tag{2.14}$$

In the case of thermal equilibrium, carrier concentration is independent of time. The process of recombination and generation of carriers are equal. i.e,

$$G_{n_0} = G_{p_0} = R_{n_0} = R_{p_0} \tag{2.15}$$

Where G is the generation rate. and R is the recombination rate in units of cm^{-3} s^{-1}. The subscripts n and p denote electron and hole, respectively. In cases of external excitations (like a flux of photons), the number of electrons and holes can increase or decrease with respect to equilibrium case.

$$G_{n_0}\ n = n_0 \pm \delta n \ and\ p = p_0 \pm \delta p \tag{2.16}$$

For carriers in equilibrium, the rate of generation of carriers and recombination of carriers are independent of time. Meanwhile, the recombination and generation rates for excess carriers change with time. The recombination mechanisms are explained in subsequent sections.

2.6 Recombination Mechanism

Only the photons having larger energy than the material's bandgap, excites the electrons from valence band to the conduction band. It is ideal for all such excited electrons to be transferred to the electrodes in a solar cell. However, the electron might return to the valence band and unite with the hole, releasing energy. This is referred to as recombination. One of the key causes of a decline in solar cell efficiency is recombination. Radiative recombination, Shockley-Read-Hall recombination, and Auger recombination are the three forms of recombination (J. A. Nelson, 2003).

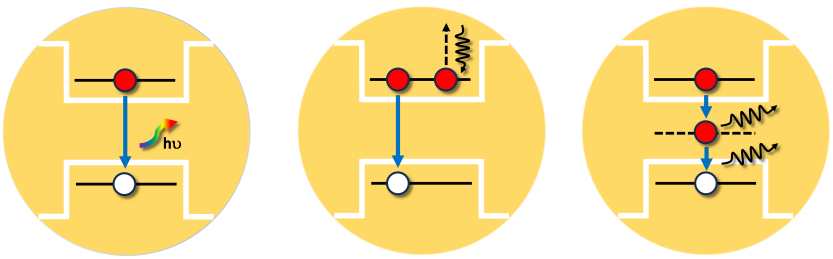


***Figure* 2.4** Schematics of Recombination mechanism a) Radiative recombination where emission of photon is visible b) Auger recombination where three carriers are involved c) SRH recombination which is accompanied by trap states.

2.6.1 Radiative Recombination

When an electron in the lowest conduction band recombines with a hole in the highest valence band, this type of recombination happens. For semiconductors with direct bandgap, this process is accompanied by the release of a photon of energy E_g, equal to the energy difference between these states. For the case of semiconductors with indirect bandgap, the electrons in the conduction band change momentum to reach the top of the valence band by releasing a phonon and then recombine with holes in the valence band by releasing a photon. The net recombination rate in its simplest form can be described as (Christoph Alexander Meßmer, 2022):

$$R_{rad} = C_{rad} \,.\, (np \; - n_i^2 \,) \tag{2.17}$$

Where C_{rad} is a material-specific constant, n_i is the effective intrinsic density, n and p are the local electron and hole densities, respectively.

2.6.2 Auger Recombination

In Auger Recombination, an extra electron participates in the recombination process in addition to the electron-hole pair. The excited electron returns to the valence band to recombine with the hole, but the surplus energy is used to excite another electron in the conduction band. This other electron then deexcites to the conduction band edge by releasing heat energy. This non-radiative process is a three-particle process with a net recombination rate of as (Christoph Alexander Meßmer, 2022);

$$R_{auger} = \left(C_n n - C_p p\right).\left(np - n_i^2\right) \tag{2.18}$$

Where C_n and C_p are auger coefficients that vary with temperature. Auger recombination is typically dominant in high excess carrier concentrations and indirect semiconductors such as silicon. Extrinsic recombination processes were mostly circumvented and silicon's intrinsic limit was approached further thanks to improvements in passivation techniques, greater characterization, and the overall quality of silicon bulk materials over the past decade. Richter et al. released a silicon intrinsic recombination model in 2012 that covers a wide range of doping and carrier injection levels (Richter et al., 2012).

2.6.3 Shockley-Read-Hall (SRH) Recombination

SRH recombination is also known as non-radiative recombination. In this process, electrons from the conduction band reach the valence band in two steps. In the first step, the electron deexcites to a defect level within the bandgap region by releasing a photon or a phonon (Hall, 1952; W. Shockley & Read, 1952). Although the defect energy level is dependent on intrinsic properties and doping properties for general modelling, a defect level in the middle of the bandgap is considered. In the next step, the electron further deexcites to the valence band by further releasing energy.

The net recombination can be expressed by;

$$R_{SRH} = \frac{np \; - n_i^2}{\tau_n(n + n') + \; \tau_p(p + p')} \tag{2.19}$$

With

$$n' = n_i \exp\left(\frac{E_T}{k_B T}\right) \;\; and \; p' = n_i \exp\left(-\frac{E_T}{k_B T}\right) \tag{2.20}$$

Where n_i is the effective intrinsic density, and E_T is the trap level energy with respect to the intrinsic energy level.

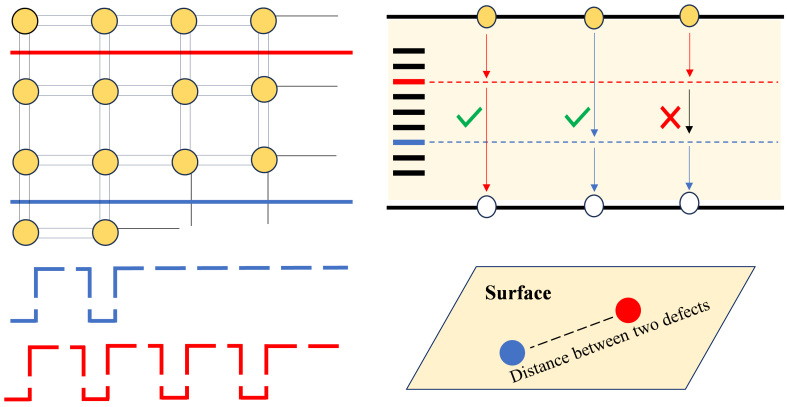


Figure 2.5 Schematic to highlight interface recombination. The Bloch potentials change near the surface, creating new energy levels within the bandgap region. An electron does not hop into energy levels that are close as the defects itself (red and blue) can physically be far away.

In the interfaces of layers of solar cells incomplete bonds are present. Thes incomplete bonds acts as a trap for photogenerated carriers. The loss of carriers due to shape and orientation of lattice is called interface recombination loss. These trap states have different energy levels based on the surface where the bond is broken. In the figure above two energy levels are shown using red and blue lines. The Bloch like potentials change in the interface and thus the eigen values are changed in the interface. The carriers may only hop into one of the states even if trap states are close energetically before reaching the conduction or valence band. This is because even if states are nearby energetically, they can be far away physically.
Total interface recombination can be expressed as:

$$R_{iF} = \frac{S_n\ S_p\left(np - n_i^2\right)}{S_n\ (n + n_1) + S_p\ (p + p_1)} \tag{2.20}$$

Here, $p = N_v\ e^{-(E_{iF} - E_{(V,iF)})/kT}$ and $n = N_C\ e^{-(E_{(c,iF)} - E_{iF})/kT}$ are the emission rates of electrons and holes from defect states. In the above expression, S_n and S_p represent the hole interface recombination velocity and electron interface recombination velocity, respectively. Interface recombination speed for electron $S_n = v_{th}\,\sigma_n N_t$ and $S_p = v_{th}\,\sigma_p N_t$ for holes depend on the number carriers on the interface and the thermal velocity of respective carriers. Since trap states at interface reduces V_{oc} drastically, it is very important to mitigate its effect. One of the effective solutions is to band engineer cautiously and introduce a small positive conduction band offset between the absorber and buffer layers. Due to this offset, the electrons cannot flow easily to the buffer layer; as a result the recombination of carriers is drastically reduced.

2.7 Charge Carrier Transport Equations

Considering the special form of Poisson equation derived from the Maxwell equations, which correlated the potential ϕ times the permittivity ε to the charge-carrying quantities like donor concentrations N_D, acceptor concentrations N_A, and free electron and hole density n, p (Altermatt, 2011);

$$\nabla.\,(\varepsilon\ \nabla\Phi\ ) = -q\ (p - n + N_D - N_A), \tag{2.21}$$

And the continuity equations, which involve variation in electron and hole densities with their current densities J_n and J_p, and generation rate G and recombination rate R are given as;

$$\frac{\delta n}{\delta t} = \frac{1}{q} \nabla J_n + G - R, \tag{2.22}$$

$$\frac{\delta p}{\delta t} = -\frac{1}{q} \nabla J_p + G - R, \tag{2.23}$$

with the drift-diffusion approximation;

$$J_n = -q\mu_n n \nabla\Phi + q D_n \nabla \mathrm{n} \tag{2.24}$$

$$J_p = -q\mu_p p \nabla\Phi + q D_p \nabla \mathrm{p} \tag{2.25}$$

The solution of equations yields the electron and hole densities n(x,t), p(x,t), and the electric potential ϕ(x,t) from which other quantities can be derived, such like band diagrams, local recombination rates cell currents and phases shift.

2.8 Absorption of Light and Transmission loss-mitigation

When Light from the sun hits the p-n junction solar cell, photons with energy less than the absorber's Bandgap (E_g) does not change the cell's electrical output power and transmit throughout the cell. As a result, only a selected part of broad solar spectrum is used for energy conversion while the rest of spectrum remains unutilized. Photons having energy larger than the E_g contribute in the output, but still some amount of photon energy beyond E_g will simply be lost as heat.

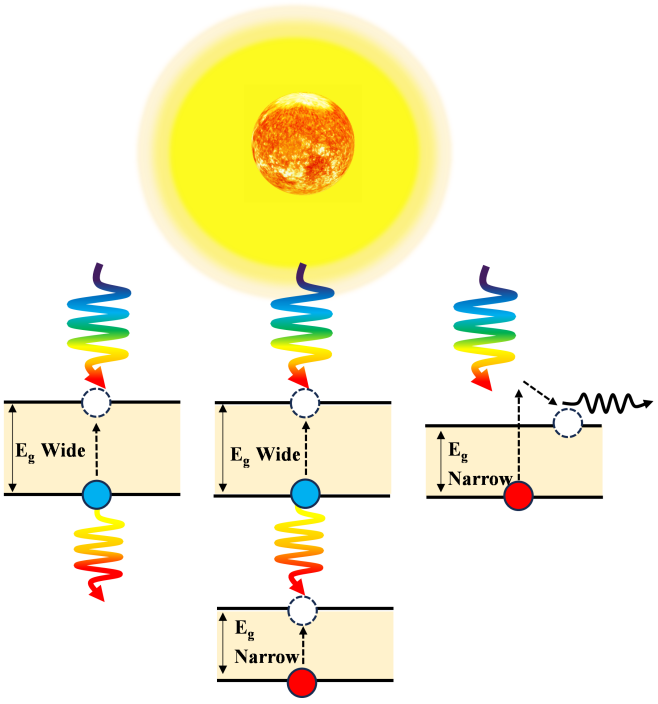


Figure 2.6 The need for light management in solar cell. In wide bandgap materials low energy photons are unutilized. In narrow band gap materials hot electrons take away energy. In tandem solar cells the residual spectrum after passing through wide bandgap materials are utilized by narrow bandgap materials.

Approaches, like multiple junction or tandem junction solar cells and graded bandgap absorber are rigorously adopted for minimizing the transmission losses in the solar cell devices. Tandem solar cells are the arrangement of stacking the high bandgap top cell above the low bandgap absorber-based bottom cell so that the lower bandgap bottom absorber absorbs the lower energy. Similarly, by introducing bandgap grading in absorber material one can mitigate

the transmission loss of the solar spectra for better device output. In general, tandem cells can be made in two ways: one form is two terminal (T) cells and the other four T cells. The highest theoretical power conversion efficiencies (PCEs) for 4T and 2T configurations of two-junction TSCs, with typical light intensity (1 sun), are 46% and 45.7%, respectively.

2.9 Thin-film Solar Cell

Thin-film solar cells are thought to be a strong alternative to Silicon-based solar cells. Unlike the process of creating a silicon wafer, which involves slicing a massive block of crystalline silicon, producing thin films involves coating or depositing the material of interest onto a substrate. The temperature range that is used to produce the absorber layer is another point of difference. Processing temperatures for thin film solar cells typically stay below 600 °C, but for high-quality silicon wafers, they can reach 1000 °C. Usually, materials chosen for thin film solar cells are of direct band gap nature and have a high absorption coefficient. This provides an advantage to fabricate thinner devices, the opportunity to reduce cost involved with material involved and a possibility to increase efficiency. The commercially available thin film technology such as Cu(In, Ga),Se_2 (CIGS) and CdTe based solar cells have touched the record efficiency of 23.35% (Chantana et al., 2020) and 22.1% (Green et al., 2018). In theory, CIGS-based CdTe solar cells have a greater maximum value than silicon-based solar cells, but in practice, they have not been able to achieve efficiency levels comparable to silicon-based cells.

2.10 Quaternary Chalcogenide Solar Cell

Because Cd is hazardous in CdTe solar cells and Indium is scarce in CIGS solar cells, a research effort to create replacements to these two elements is still ongoing. Solar cells based on Cu_2ZnSnS_4 (CZTS) are an alternative to CIGS and CdTe technologies. CZTS is a member of the unique quaternary family A_2BCD_4 (where A = Cu, Ag, B = Zn, Ni, Co, Fe, Mn, Cd, Hg, Ba, Sr group II elements, C = Si, Sn, Ge, and D = S, Se) with outstanding solar cell performance. These materials are prospective candidates for solar cells due to their high absorption coefficient (> 10^4 cm^{-1}) and tunable bandgap in the range of 1.0-1.5 eV, which is thought to be beneficial for solar cell performance. At both the atomic and device levels, the structure is remarkably similar to CIGS. Zn and Sn have taken the position of In and Gallium. Kesterite CZTS-based solar cells are manufactured in the same device stacking as CIGS solar cells. Thus, there is hope that CZTS can be scaled in the same way as CIGS can. Furthermore, the greatest efficiency CZTSSe achieved is 13.8%, which is still far from the 23.35% (Chantana et al., 2020) efficiency of its equivalent chalcopyrite CIGS solar cell, while the theoretically projected SQ limit is ~32%. The lower short circuit (Jsc) performance of a solar cell than the SQ limit is due to improper absorption of incident radiation or partial extraction of photogenerated carriers at the electrodes, whereas the reduced open-circuit voltage and fill factor demonstrate photogenerated carrier recombination in bulk as well as at interfaces, as well as parasitic resistance.

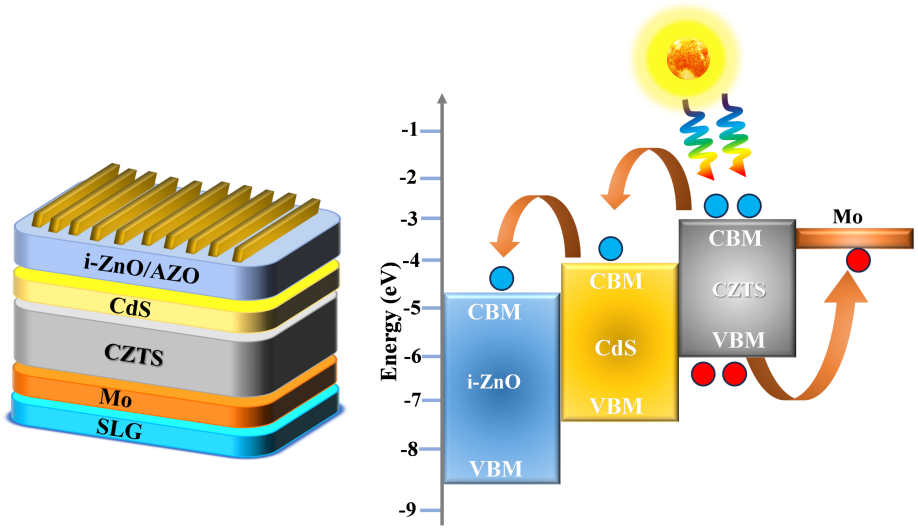


Figure 2.7 The standard device architecture of the CZTS solar cell. The band alignment (on right) shows the movement of the photoexcited electron (cyan ball) and holes (red balls).

Figure 2.7 depicts the typical device architecture of a CZTS solar cell, together with band alignment, which is based on the highly successful CIGS device architecture, with CIGS substituted with CZTS. The substrate in the device is soda lime glass (SLG), and on top of it, Mo is back contact, followed by a light absorber layer of CZTS. Then, CdS and ZnO are stacked as buffer and window layers. The top surface is covered with an i-ZnO/AZO layer and a contact grid. When the light is turned on, the photogenerated carriers move in the opposite direction, so that the electron travels from CZTS's CBM to CdS and then through i-ZnO gathered on the top contact. The hole that runs from CZTSs VBM to the back contact side is collected. The efficient collection of carriers at the electrodes is a vital factor that determines the majority of the system's performance. The CZTS solar cell is made up of several interfacial layers through which photogenerated carriers must pass before being collected at the end of the metal contacts. Because of the high defect density at the CZTS/CdS interface, the potential of carrier recombination increases, resulting in a low open circuit voltage. Another cause of Voc deficiency is incorrect band alignment at the CdS/CZTS interface (Kumar et al., 2015). Secondary phase development during material manufacturing degrades device performance as well. The non-stoichiometric CZTS causes secondary phases, lattice defects (vacancies, interstitials, antisite), defect clusters, and a significant open circuit voltage deficit, as defined, $E_g/q - V_{OC}$, where Eg is the absorber's bandgap and q is electron charge.

In addition, The V_{OC} deficit for CZTS solar cell can be more than 650 mV while it's counterpart CIGS cells have 500 mV value. The main cause of Voc deficit is the non-radiative recombination induced by the bulk defects in absorber and interface. In CIGS, the antibonding coupling of Cu d^{10} with Se p orbitals raises the valence band maximum (VBM), creating Cu vacancy a shallow acceptor, a dominant defect in CIGS. In CZTS also consists the Cu d^{10} element and the V_{Cu} as a shallow acceptor (Hong et al., 2016b). But other possible antistites defects – Cu at Zn site (Cu_{Zn}) also appears as deep acceptor with lower formation energy. This is because of small size mismatch in Cu^{+1} (0.91 Å) and Zn^{2+} (0.88 Å) ions. Similarly, Sn^{4+} (0.83 Å) and Zn also have small size mismatch leading to antisite Zn_{Sn}.

Further, An. Et al. reported that in $Cu_2ZnSn(S_xSe_{1-x})_4$, the Cu-Zn disorder in different planes (i.e., Cu-Sn and Cu-Zn) is more detrimental than the case when the disorder lies in the Cu-Zn plane because it elongates the Sn-S/Se bond length and, hence, downshifts the conduction band, decreasing the band gap and reducing the optical absorption (Zhu et al., 2024). Therefore,

CZTS shows higher non-radiative recombination than CIGS. And due to the presence of three cations with the same coordination results, the formation of many defects and defect clusters resulting from solar cells has a huge Voc deficit. To overcome this issue, the element with larger size mismatch with Cu, such as Be, Ca, Sr, and Ba, can replace Zn in CZTS. However, a drawback with large size mismatch is the instability of material in the kesterite phase.

Table 2.1: A comparison among the reported quaternary chalcogenide based solar cell.

S.No.	Absorber	PCE (%)	V_{OC} (V)	J_{SC} (mA/cm^2)	FF (%)	E_g (eV)	Ref.
1.	Ag-doped $Cu_2ZnSn(S/Se)_4$	13.8	0.551	35.74	71.7	1.097	(P. Chen et al., 2023)
2.	$Cu_2ZnSnSe_4$	12.5	0.491	37.37	68.2	1.04	(J. Li et al., 2020)
3.	Cu_2ZnSnS_4	11	0.731	21.74	69.3	1.5	(Yan et al., 2018)
4.	$Cu_2(Cd,Zn)SnS_4$	12.6	0.64	27.8	71	1.34	(J. Li et al., 2020)
5.	Cu_2CdSnS_4	7.96	0.624	22.3	57.2	1.42	(Hadke et al., 2019)
6.	$Ag_2ZnSnSe_4$	5.18	0.504	21	48.7	1.35	(Gershon et al., 2016)
7.	$Cu_2ZnGeSe_4$	8.5	0.625	24.4	55.7	1.4	(Choubrac et al., 2020)
8.	$Cu_2BaSn(S,Se)_4$	5.2	0.611	17.4	48.9	1.55	(Gershon et al., 2016)
9.	Cu_2MnSns_4	0.56	0.345	4.5	38.1	1.6	(Lie et al., 2022)
10.	Cu_2SrSnS_4	0.48	0.181	9	34.4	1.88	(Lie et al., 2022)

In the last few years, researchers have synthesized Cu_2BaSnS_4 and Cu_2SrSnS_4 and other quaternary chalcogenide thin films and also explored the possibility of solar cells (Lie et al., 2022). Some of these are tabulated in Table 2.1 with their performance metrices and bandgap. We see Ag doped CZTSSe based device shows larger efficiency where authors report relatively lesser deep level defect and hence larger Jsc, Voc and fill factor for efficient outcome. In addition, all the materials have bandgap value with in the range 1.04 to 1.55 which was derived by taking the first derivative of the EQE curve in the long wavelength. We find CZTSSe based absorber as most efficient one, which has been under exploration for a long time compared to others. However, due to various influences of sample type, quality, measurement method and the associated uncertainties, more measurements are required with other materials to build up a consistent picture. Further, we see Cu_2HgSnS_4 a possible absorber material due to its reported bandgap value of 1.33 eV, which is also suitable for solar applications. While studying the literature, we see this material is mainly unexplored from the energy aspect. Computational modelling of this material and possible S and Se alloy composition would give an idea to realize this for photovoltaics. Further device modelling could also be beneficial for understanding carrier transport and band alignment, considering the proper defect and carrier concentration.

2.11 Thermoelectric Motivation and Applications

Meeting the world's energy demand in an eco-friendly manner can be achieved through the exploration of renewable energy sources and the promotion of efficient energy consumption practices, such as the recovery of waste heat. Thermoelectric materials have garnered considerable interest for their potential in waste-heat recovery. Thermonuclear power for space

missions (Zinkle & Was, 2013), vehicles (J. Yang & Stabler, 2009), manufacturing procedures, nuclear and oil and gas remote sensing, etc. using thermoelectric materials are among these uses (J. Chen et al., 2016). Another practical use of thermoelectric materials is solid-state refrigeration. This is advantageous in settings where spot-cooling or heating needs to be precisely controlled or where the vibrations linked to conventional refrigeration methods are detrimental, such as in medical storage or wine refrigerators. The extensive academic and scientific influence and diverse range of possible uses of thermoelectric materials in the past 50–60 years has made them a hot topic in many disciplines, such as solid-state chemistry, metallurgical procedures, and thermal/electronic transport processes.

Thermoelectricity, which can be defined in terms of the Seebeck, Peltier, and Thomson effects, is the direct transformation of heat into electricity and vice versa. A voltage differential (ΔV) generated by a shift in temperature (ΔT) across the material is known as the Seebeck effect, which was first observed in 1821 by the German physicist Thomas Johann Seebeck (Snyder & Ursell, 2003). Because of the imposed temperature gradient, the majority charge carriers diffuse from the hot side to the cold side, creating the voltage differential. The Seebeck coefficient ($S \approx -\Delta V/\Delta T$) or thermopower, an intrinsic feature of the materials, is the ratio of the produced voltage gradient to the temperature gradient. The Peltier effect is the inverse phenomena of the Seebeck effect, which was discovered in 1834 by the French physicist Jean Charles Athanse Peltier. Heat absorption or rejection (Q) arises from the application of an electrical voltage across the materials, depending on the direction of the current (I). The Peltier coefficient $\pi_{ab} = Q/I$, and the Seebeck and Peltier coefficients are connected by the Kelvin relationship; $S_{ab} = \pi_{ab}/T$. All materials used in thermoelectric power production and cooling applications exhibit the Seebeck and Peltier phenomena (Hamid Elsheikh et al., 2014). The theory put forth by William Thomson, known as the Thomson effect, holds that materials can be reversibly heated or cooled when an electric current is present and a temperature gradient is also present. In terms of energy conversion, the Thomson effect plays no role at all.

In the dimensionless figure of merit, $ZT = S^2\sigma T/\kappa$, the Seebeck coefficient (S), electrical conductivity (σ), thermal conductivity (κ), and absolute temperature (T) are used to index the conversion efficiency of thermoelectric materials. The electronic component κ_e and the lattice vibration portion κ_l are both comprised in the overall thermal conductivity κ. Since most of the involved quantities are interdependent therefore tuning one to achieve higher ZT value is a complex task. Generally, Phonon Glass and Electron crystal analogy is said as ideal for the best thermoelectric material where glasslike low thermal conduction along with crystal-like large electrical conductivity enhances the figure of merit (Snyder & Toberer, 2010). In order to achieve a higher rate of converting heat to electricity. several strategies are followed in material engineering.

2.12 Critical Features Required for Effective Figure-of-Merit

For the TE material, over the past years, various strategies have been applied to improve ZT value (Jia et al., 2022). Optimizing carrier concentrations (n) and applying band engineering to decouple σ and S while concurrently increasing their values are the most effective methods for improving electrical transport and obtaining overall high $S^2\sigma$. Moreover, the lattice thermal conductivity (κ) can be reduced effectively through nanostructure and defect engineering, without sacrificing the electrical transport of TE materials (Qu et al., 2021; Zheng et al., 2021) . Therefore, the enhanced ZT can be ultimately achieved. These approaches are discussed in the following sub-sections:

2.12.1 Optimizing carrier concentration (n)

All the parameters that affect the TE performance such as S, σ and κ_e are directly correlated with the carrier concentration through the following relations (L. Yang et al., 2018);

$$S = \frac{8\pi^2 k_B^2}{3eh^2} m_d^* T \left(\frac{\pi}{3n}\right)^{\frac{2}{3}} \quad ; \quad \sigma = ne\mu \quad ; \quad \kappa_e = ne\mu LT \tag{2.26}$$

Where $m_d^* = N_V^{2/3} m^*$ is the density of states effective mass of carrier, e is the electrical charge of the electron, k_B is the Boltzmann constant, μ is carrier mobility, L is Lorenz number, N_v is orbital degeneracy and m^* is average effective mass of degenerate valleys. These relations suggest that optimizing n is a crucial strategy to gain high σ and S as well as low κ_e so that device can achieve high ZT value. According to the experimental findings, getting the ideal carrier concentration (n*) for any TE material requires fine-tuning the n. The n* value is quite sensitive to temperature and material properties. As per the single-band model, $n^* \propto (m_d^* T)^{1.5}$ relation is suggested to predict n*, where m_d^* varies with different band structure (Y. Xu et al., 2017). Pei at al, studied La-doped and I-doped PbTe systems, confirming that this above formula of n* can be used to accurately calculate n* for PbTe-doped system (Pei et al., 2012). Because m_d^* value is generally small, therefore temperature becomes the dominant parameter to control n*. This information is highly useful to determine the optimal application temperature for evaluating n* for various materials.

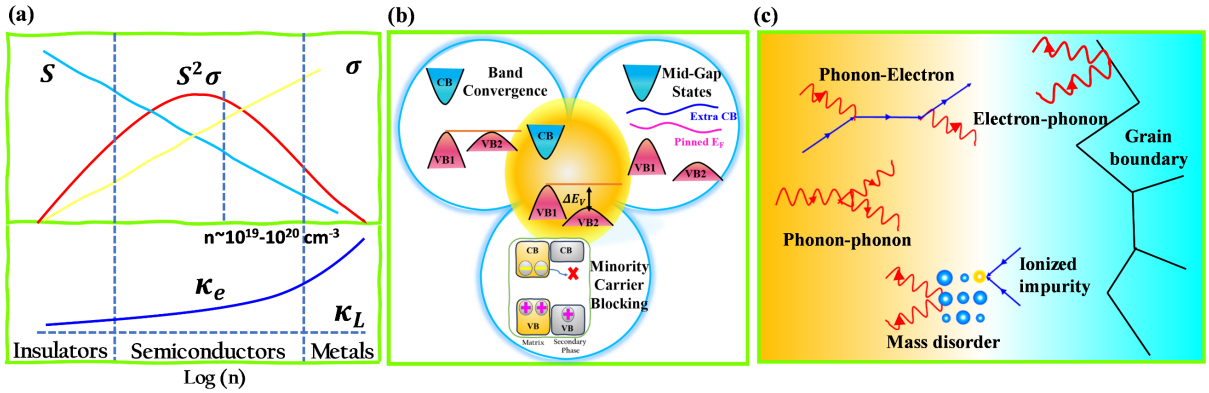


Figure 2.8 A schematic representation of (a) carrier density dependent variation in S, σ, κ_e. (b) Multiple band engineering techniques for achieving higher ZT. (c) Various scattering phenomenon for phonon and electron in the system.

2.12.2 Band structure Dependence

The band structure of a material influences how well it conducts electrical transport; hence TE performance can be engineered by modifying the band structure. The following are the steps involved in band engineering for TE materials: (a) Increasing E_g to stabilize n; (b) adjusting m* or reaching a resonant state close to the Fermi level to enhance S; and (c) attaining band convergence can also enhance S and σ.

(a) Tuning the band gap

The thermal excitations of minority carriers at elevated temperatures (T) have the potential to augment the overall n and lead ZT reduction as a result of S reduction and enhancement κ_e as per equation 2.26. Theoretical and experimental research indicates that Eg can be tuned through doping, and an increase in Eg can cause the thermal excitation temperature of minority charge carriers to move toward higher temperatures, hence suppressing the minor carriers. The minority charge carriers reduce ZT by acting as heat carriers, which results in bipolar thermal conductivity (κ_{bi}) contributing total κ. The κ_{bi} is defined as $\kappa_{bi} \propto \exp(-E_g/2k_BT)$, which increases with temperature. This effect becomes apparent at intermediate and higher temperatures, which reduces the ZT of TE materials. In contrast, for large bandgap values the κ_{bi} value can be reduced by avoiding the minor carrier's excitations even at high temperatures.

(b) Electronegativity differences and carrier mobility

For exploring new TE materials, the average electronegativity difference of the constituent elements should be ≤ 0.5 (D.M.Rowe, 1995). It is a limit for the charge transfer between the cations and anions and to ensure that their interacting orbitals are in similar energy range for more efficient overlap, which will result in sharper bands in the electronic band structure. For the carrier effective mass, $m^* = \frac{\hbar^2}{d^2E/dk^2}$, represents if the sharper curvature will reduce m^*, leading to higher charge carrier mobilities. Additionally, the weighted mobility, $\mu\left(\frac{m_d^*}{m_e}\right)^{\frac{3}{2}}$, where μ denotes the mobility of carriers and m_e is the electron mass, is a primary determinant of the thermoelectric semiconductor to obtain effective thermoelectric device. But for bands with a large mass m_b, μ remain small. It is expected that $\mu \propto {m_b^*}^{-\frac{5}{2}}$ which is most prevalent on good thermoelectric materials, for charge carriers that are mainly scattered by acoustic phonons.

(c) Crystal symmetry and Band Convergence

For the effective electronic transport in a material, multiple bands could be advantages if the edges of the other highest bands lie within a minimum energy range (≤ 0.1 eV) of VBM (for p-type) or CBM (for n-type). Such bands are called degenerate and can be explained by the effective band degeneracy or multiplicity (N_V^*). It is possible to raise Nv by achieving the convergence of various electronic bands in materials through appropriate doping, increasing T, or modifying crystal symmetry. Additionally, for band converging at same k-point render stronger intervalley scattering relative to bands at distant k-point (J. Park et al., 2021). The Seebeck coefficient and electrical conductivity exhibit an inverse relationship with respect to m^*. A lesser value of m^* is advantageous for σ but detrimental for S. Conversely, a high multiplicity enhances S with a small compromise to σ, thereby resulting in an increased power factor (PF).

Materials having higher symmetric crystal structures such as Cubic PbTe or Hexagonal Bi_2Te_3 have naturally high N_V^* when VBM or CBM lie on or between high symmetry point on the Brillouin zone, as there are effectively many symmetrically identical duplicates of such bands. By doping, we can increase the multiplicity by tuning the lattice parameters to improve the symmetry of crystal, such that non-degenerate bands are shifted to be closer in energy to the VBM or CBM. For example, in chalcopyrite $CuInTe_2$, substitutional point defects Ag_{Cu} or Ga_{In} were used to transform the distorted tetragonal into a pseudo-cubic lattice (H. Kim et al., 2021).

2.12.3 Low Lattice Thermal Conductivity

Having materials with low heat conductivity is crucial for obtaining high thermoelectric figures of merit. Activating phonon scattering at many length scales while keeping charge carrier transport intact is one approach. Minimizing heat transport is accomplished by reducing the size of the crystal domain to the nanoscale (1-100 nm) or by introducing phonon scattering centres on the scale of an atomic length scale, like vacancies or rattling atoms. Additionally, the potential decoupling of the Seebeck coefficient and electrical conductivity is enhanced by limiting the lattice size to the nanoscale.

(a) Structural anharmonicity in the crystal

Phonon vibrations are composed of both anharmonic and harmonic constituents. In the harmonic vibration mode, the lattice vibration exhibits non-interactive and decay less propagation. The divergence from harmonic vibration mode disrupts the inherent characteristics of normal thermal transport and serves as a foundation for phonon damping and phonon group velocity slowing. The quantification of anharmonicity is generally done using the Gruneisen parameter (γ). An ideal harmonic crystal is denoted by γ=0, but any non-zero value signifies

anharmonicity (Morelli et al., 2008). A positive or negative number value of γ indicates the phonon frequency softening and hardening with expansion of lattice. Generally, the thermal conductivity relates to γ in the following way;

$$\kappa_l = \frac{M\ v_m^3}{TV^{\frac{2}{3}}\gamma^2}\left(\frac{1}{N^{\frac{1}{3}}}\right) \tag{2.27}$$

In this case, M represents the average mass, v_m denotes the mean speed of sound, and γ is the Gruneisen parameter and primitive unit cell has N atoms, and V is the average volume per atom. A larger value of γ, in general, results in greater anharmonicity and, as a result, poorer lattice thermal conductivity. Chemical bonding and lattice periodicity are also the important factors, which play a key role in the phonon dynamics. Soft bonding and lone pairs are found leading to hindering the thermal transport. In addition, the antibonding states in the valence band are also found supporting lower thermal conduction by introducing instability in the system. For layered structure the weak inter-layer interactions can be exceptionally beneficial for poor thermal transport while intralayer interaction leads superior electronic transport (Z. Yang et al., 2023).

(b) Microstructural defects for lattice thermal conductivity reduction

Microstructural defects scatter the phonon and reduces their relaxation time, which will further reduces lattice thermal conductivity (Huang et al., 2023). However, thermal transport through the lattice occurs thorough the propagation of phonons at varying frequencies. At low temperatures, the thermal conduction occurs through low frequency phonons because available thermal energy is not sufficient to excite the high frequency phonons. At the high temperature, there is enough energy to excite the high frequency phonon which dominates the thermal transport. The zero-dimensional defects (0D) such as vacancies, antisite defects, substitutional defects, discordant atoms, mainly scatters the high frequency phonons. While 2D interface defects like grain boundaries and the interface with secondary phase can scatter low-frequency phonons, one-dimensional (1D) defects like dislocations can scatter mid-frequency phonons. Therefore, a TE material having all these defects can effectively scatter phonon across a wide range of frequencies, leading to low lattice thermal conduction for a range of temperature and in results improves ZT.

2.13 Quaternary Chalcogenides as Thermoelectric Devices

Cu-based Quaternary chalcogenides have already been proven to be suitable for photovoltaics. Because these compounds have strong covalent bonds, it is presumed that they have high heat conductivity and are unsuitable for thermoelectric applications (Qu et al., 2021; Shin et al., 2017). Numerous research indicating enhanced mobility and reduced thermal conductivity have recently upended this idea. Cu-based tellurides and selenides, in particular $Cu_2HgGeTe_4$ and Cu_2GeSe_4, have recently been achieved with high carrier mobility and low thermal conductivity (Qu et al., 2021). With the added benefit of these quaternary compounds' complicated structures in terms of decreased thermal conduction, their varied cationic valences give opportunity of managing their fermi level by modifying their cation ratios. In addition, certain Adamantines with atomic configurations I_2-II-IV-VI_4 that crystallise in the stannite phase exhibit suitable structural stacking, enabling the separation of electrical conductivity from thermal conductivity and the Seebeck coefficient. A suitably wide bandgap feature in these family materials further aid in avoiding the bipolar effect present in traditional materials causing reduced thermoelectric performance. Interestingly the close proximity of multiple cations ordering motifs provide ground for disorder which impact on optical and electronics properties in the sulphide and selenide results a challenging for photovoltaic community however opportunity to leverage the transport and reduce the lattice thermal conductivity. Several materials like Cu_2ZnSnS/Se_4, $Cu_2FeSnSe_4$, $Cu_2CdSnSe_4$, $Cu_2ZnGeSe_4$ are studied for thermal

transport and mentioned that the quaternary materials do possess significantly reduced lattice thermal conductivity as compared of the binary and ternary counterparts (Heinrich et al., 2014; F. S. Liu et al., 2014). Several strategy like nano structuring as in $Cu_2HgSnSe_4$ nanoparticles, alloying in $CuPbSb(S_{1-x}Se_x)_3$ and $Cu_2CoSnS_{(4-x)}Se_x$, doping in $Cu_2CdSnSe_4$ with Mn atom (F. S. Liu et al., 2014) etc. Similarly, $Cu_2CoSnSe_xS_{4-x}$ is also demonstrated with enhanced power factor with 0.75 ZT value for intermediate temperature (Parashchuk et al., 2023). A record ZT of ~ 1.6 is reported for Na-doped p-type CZTS single crystal having thermal conductivity of ~ 0.94 W m^{-1} K^{-1} at ~800K (Nagaoka et al., 2021b).

While comparing the available literature chalcogenide and other known thermoelectric as shown in Table 2.2, we see that the quaternary chalcogenide is revealed suitable for intermediate (500 – 700 K) and high temperature (> 700 K) range. However earliest and most utilized chalcogenides thermoelectric material Bi_2Te_3, Bi_2Se_3, along with newly explored SnSe, HgSe, Ag_2Se, and their doped variant are known for low temperature (300 -500 K) applications due to their higher power factor along with ultralow κ_l (< 1 W m^{-1} K^{-1}) within low-temperature range. Interestingly, instead of any heavy element in SnSe, the layered crystal structure and anharmonicity are the key reasons for equipping this material with good thermoelectric with lower heat conduction. As a result, till now, ~2.8 ZT is reported for n-type SnSe crystal, which is observed as the maximum ZT at 773 K among all known thermoelectric materials (Chang et al., 2018). Additionally, GeTe, Cu_2Se, and their alloy and nanostructures are also found applicable for intermediate temperature range. Skutterudite compounds like $Ba_{0.08}La_{0.05}Yb_{0.04}Co_4Sb_{12}$ where host-cage structure kind entity is found rattling feature which reduces thermal conduction and are known for high temperature thermoelectric. Additionally, for flexible electronics and thermoelectric device fabrication, the materials are required to have significant elastic strength and not be brittle. Several materials are also highlighted in the Table 2.2, showing flexible thin film and thermoelectric device opportunities. Chalcogenides are also seen as fulfilling this requirement and therefore, have also been studied in this aspect.

Table 2.2: Multiple chalcogenides based thermoelectric performance for multiple temperature.

S. No.	*Material*	*Type*	*ZT*	*T (K)*	*σ* (*S* m^{-1})	*S* (μ*V* K^{-1})	*PF* (μ*W* cm^{-1} K^{-2})	k_l (*W* m^{-1} K^{-1})	*Ref.*
1	$Bi_{0.5}Sb_{1.5}Te_3$	p	~1.86	320	650.0	~242	~38.1	~0.65	(S. Il Kim et al., 2015)
2	Cu_2Se	p	~1.82	850	~100.0	~300	~9.0	~0.37	(K. Zhao et al., 2017)
3	$Ge_{0.9}Sb_{0.1}Te$	p	1.85	725	~815.0	~250	~51.0	~1.90	(Bayikadi et al., 2020)
4	$SnSe_{0.97}Br_{0.03}$	n	2.8	773	~40.9	~−477.4	~9.3	~0.25	(Chang et al., 2018)
5	nanoporous SnSe	p	1.7	823	53.5	307.4	~5.1	0.24	(Xiaolei Shi et al., 2018)
6	$PbTe_{0.7}S_{0.3}$ + 2.5% K	p	~2.24	823	~157.1	~310	~15.1	~0.60	(Wu et al., 2014)
7.	$Ba_{0.08}La_{0.05}Yb_{0.04}Co_4Sb_{12}$	n	1.7	850	~1340.0	~−195	~51.0	~2.60	(Xun Shi et al., 2011)
8.	Cu_2ZnSnS_4-Na-doped	p	1.6	800	~170	345	1.8 mW	~1	(Nagaoka et al., 2021b)
9.	$Cu_2CoSnSe_4$		0.75	773		~240	6	0.7	(Parashchuk et al., 2023)
10.	$Cu_2FeSnSe_4$		0.34	800	0.6×10^4	220	3.5	~1	(Dong et al., 2015)

11.	$Cu_{2.15}Cd_{0.85}SnSe_{3.9}$	p	0.71	685	~6000	~175		~0.23	(F. S. Liu et al., 2014)s
12.	$Cu_{2.3}Hg_{0.7}SnS_{3.8}$-NP	p	0.2	723	~10^4	150		0.5	(W. Li et al., 2013)
Flexible Thermoelectrics									
13.	Bi_2Te_3 +CNTs	n	0.89	300	524	-172	15.5	0.52	(Jin et al., 2019)
14.	Au-doped CNTs	p	0.203	300	1150	150	25	3.6	(An et al., 2016)
15.	CuI	p	0.21	300	143	162	3.75	0.55	(C. Yang et al., 2017)
16.	Ag_2Se	n	0.6	300	497	140	9.87	0.478	(Ding et al., 2019)
17.	SnSe	p	1.17	300	2.4	1200	3.5	~0.09	(Rongione et al., 2019)
18.	HgSe	n	0.68	300	20.5	−518	5.5	0.24	(Choi et al., 2017)

Therefore, understanding the multiple necessary features for a good thermoelectric system and considering the available literature, we observed the requirement to further explore the Cu-based quaternary chalcogenides to design new materials. In this family of semiconductors, Cu_2HgSnS_4 seems an advantageous system in terms of the presence of heavy element Hg which could help in achieving lower thermal conduction at the same time the possibility of Cu and Hg cations substitution via another element always gives the opportunity to enhance electrical conduction. We found no article addressing these features or predicting ZT on this compound. We picked this material to understand its carrier and phonon dynamics and its impact on thermoelectric performance ZT.